Neuromorphic spintronics accelerated by an unconventional data-driven Thiele equation approach

Anatole MOUREAUX, Simon DE WERGIFOSSE, Chloé CHOPIN, Jimmy WEBER, and Flavio ABREU ARAUJO*
Institute of Condensed Matter and Nanosciences, Université catholique de Louvain,
Place Croix du Sud 1, 1348 Louvain-la-Neuve, Belgium

A hardware neural network based on a single spin-torque vortex nano-oscillator is designed using time-multiplexing. The behavior of the spin-torque vortex nano-oscillator is simulated with an improved ultra-fast and quantitative model based on the Thiele equation approach. Different mathematical and numerical adaptations are brought to the model in order to increase the accuracy and the speed of the simulations. A benchmark task of waveform classification is designed to assess the performance of the neural network in the framework of reservoir computing and compare two different versions of the model. The obtained results allow to conclude on the ability of the system to effectively classify sine and square signals with high accuracy and low root-mean-square error, reflecting high confidence cognition. Given the high throughput of the simulations, two innovative parametric studies on the dc bias current intensity and the level of noise in the system are performed to demonstrate the value of our models. The efficiency of our system is also tested during speech recognition and shows the agreement between these models and the corresponding experimental measurements.

INTRODUCTION

The need for low power and efficient hardware dedicated to machine learning has led to a new type of data processing called neuromorphic computing [1]. By taking inspiration from the brain, it tries to overcome the von Neumann bottleneck by proposing artificial neurons or synapses that are highly interconnected within a parallel architecture. Different systems are under study like photonics [2–6], memristors [7] and spintronics [8]. Among the latter, spin-torque vortex nano-oscillators (STVOs) have already been shown to be choice candidates to implement hardware neurons for machine learning applications. Thanks to their highly non-linear behavior and intrinsic short-term memory, as well as a remarkable signal to noise ratio despite their nano-metric size, several machine learning tasks such as waveform and speech recognition have been performed successfully with STVO-based neural networks [9–11]. Their small size, low power consumption and CMOS-compatibility reinforce their potential interest concerning the development of neuromorphic computing systems [9, 12].

As shown in refs. [9, 13, 14], the recognition success rate is very sensitive to the non-linear profile of the STVO as well as the noise regime. These parameters depend on both, the experimental parameters (external magnetic field and working current intensity for instance) as well as the design of the STVO itself. The simulation of such neural networks is hence of prior importance to better understand the underlying phenomena involved in their cognitive properties, and to optimize these systems before the actual fabrication. Thus, a fast and quantitative model is needed. Indeed, it would require a huge computational power and an extensive amount of time to study with micromagnetic simulations the dynamics of such oscillators as well as to test several neuromorphic architectures or input parameters that could be optimized for experimental measurements [15, 16]. Several solutions are proposed like using a model based on non-linear magnetic oscillator theory [17, 18], using machine learning to predict the dynamics of STVOs with Neural ODEs [19] or using analytical models based on the Thiele equation approach (TEA) [20, 21] for simulating STVOs.

Abreu Araujo *et al.* [18] have already compared experimental results [9] and results from STVOs simulated with the non-linear magnetic oscillator theory [17] for the recognition of spoken digit with reservoir computing. The parameters needed for the non-linear magnetic oscillator model are extracted experimentally and there is an excellent agreement between experimental and simulated results. However, the accuracy of the experimental neural network is surprisingly higher than that of the simulated neural network. On the contrary, the function given by Neural ODEs with the addition of noise allows to predict perfectly the experimental results of Torrejon *et al.* [9] with an acceleration factor of 200 compared to micromagnetic simulations [19]. Still, the function given by the neural network is a black box and one does not have access to the underlying physics of the oscillator. As an alternative, TEA models are elegant solutions that have the interest of being based on an analytical description of the underlying physics. However, they only give quantitative results for the STVO behavior in the resonant regime [22] (resp. steady-state regime [23]) *i.e.* when it does not oscillate (resp. when it undergoes stable oscillations). For the transient regime of STVOs (*i.e.* from the resonant regime to the steady-state regime or vice versa), TEA models are only able to yield qualitative results. Unfortunately, the transient regime is precisely the regime of interest for reservoir computing applications. A recent data-driven TEA (DD-TEA) model [16] has been shown able to describe quantitatively both the steady-state and transient regimes of STVOs. Furthermore, the results were obtained with an acceleration of 6 orders of magnitude compared to micromagnetic simulations, hence greatly improving the throughput of the simulations. This quantitative and ultra-fast model is simply based on TEA and a few micromagnetic simulations.

The speed of this DD-TEA model can be further improved as shown by the two analytical models proposed below. Indeed, the combination of the DD-TEA model with additional mathematical adjustments allows to solve it fully analytically.

The two resulting analytical models described later reach a 9 orders of magnitude acceleration compared to micromagnetic simulations. These two models are then applied to three tasks. The first task is a proof of concept of pattern recognition where sine and square functions have to be distinguished. The second task is a parametric study of the cognitive results depending on the intensity of the dc input current and the signal-to-noise ratio (SNR) of the system. The last task is the comparison with experimental results from Torrejon *et al.* [9], the phenomenological model from Abreu Araujo *et al.* [18], and the results from our two analytical models based on DD-TEA in the framework of speech recognition.

METHODS

The vortex core dynamics can be described by a simple harmonic oscillator equation [22] when the pulsation ω is constant and the transient dynamic factor $\Gamma \to 0$:

$$\begin{bmatrix} X(t) \\ Y(t) \end{bmatrix} = ||\mathbf{X}||\mathrm{e}^{\Gamma t} \begin{bmatrix} \sin(\omega t) \\ -\cos(\omega t) \end{bmatrix} \tag{1}$$

where $X(t)$ and $Y(t)$ are the time-dependent Cartesian coordinates of the vortex core. As both $X(t)$ and $Y(t)$ vary quickly in time, Eq. (1) can be rewritten by considering the reduced vortex core position $s(t) = \sqrt{X^2(t)+Y^2(t)}/R$ where R is the radius of the magnetic dot. This gives:

$$s(t) = s_\infty \mathrm{e}^{\Gamma t} \tag{2}$$

where s_∞ is the final reduced position of the vortex core and Γ is a constant related to the transient state of the dynamics. In reality, Γ depends on $s(t)$ and Eq. (1) admits a general solution that writes:

$$s(t) = s_\infty \exp \int_0^t \Gamma(s(t'))\mathrm{d}t' \tag{3}$$

After a few developments not detailed here, Eq. (3) can be expressed as the following ordinary differential equation (ODE):

$$\dot{s}(t) = \Gamma(s(t))s(t) \tag{4}$$

The fully analytical expression of $\Gamma(s)$ as a function of s based on TEA is given in a previous publication [22]. For the sake of simplicity, we can truncate $\Gamma(s)$ to the second order:

$$\Gamma(s) = \alpha + \beta s^2 \tag{5}$$

Both α and β are parameters that depend on the input current density J and are described as follows:

$$\alpha(J) = a_J J + a \tag{6}$$

$$\beta(J) = b_J J + b \tag{7}$$

TABLE I. Dynamical constants for the DD-TEA models in the C+ chirality

Constant	Value	
a_J	6.64	Hz cm^{2}A^{-1}
b_J	−0.43	Hz cm^{2}A^{-1}
a	−39.97	MHz
b	−25.92	MHz

where a, a_J, b, b_J are fully analytically described constants whose value is listed in Table I. Finally, by injecting Eq. (5) in Eq. (4), the following equation appears:

$$\dot{s}(t) = \alpha s(t) + \beta s^3(t) \tag{8}$$

Eq. (8) is a Bernoulli differential equation of order 3, which accepts the following solution:

$$s(t) = \frac{s_0}{\sqrt{\left(1+\frac{s_0^2}{\alpha/\beta}\right)\exp(-2\alpha t) - \frac{s_0^2}{\alpha/\beta}}} \tag{9}$$

Where s_0 is the initial reduced vortex core position at $t = 0$. The final position of s, *i.e.* when $t \to \infty$, depends on the input current density J:

$$s_\infty(J) = \sqrt{\frac{-\alpha(J)}{\beta(J)}} \tag{10}$$

Guslienko *et al.* [23] have reported a similar expression of the transient regime obtained with a different method. The simulations based on this analytical *low-order* truncated model called s-LOTEA are two orders of magnitude faster than the previous TEA-based model (DD-TEA [16]) as no ODE needs to be numerically solved. The value of $\alpha(J)$ and $\beta(J)$ can be retrieved using the same data-driven approach as for the DD-TEA model [16], by fitting the results of a few micromagnetic simulations (performed using mumax^3 [15]). This leads to a precise description of the transient and steady-state regimes. This model hence combines physical foundations and the precision of a data-driven method.

The second model is an extension of the first one, allowing to capture any additional non-linearity in the dynamics of the vortex core that would not be accounted for in Eq. (9) due to the truncation to the second order of the $\Gamma(s)$ parameter. To do so, a purely mathematical adjustment is brought to the s-LOTEA model. Indeed, Bernoulli differential equations such as Eq. (8) can involve any real power. Hence, Eq. (9) can be generalized to the order n to write Eq. (11), where $n(J)$ is a fifth-order polynomial of the current density J injected into the STVO, whose coefficients have been determined by fitting to micromagnetic simulations results. This model was hence called the *s-analytical High-Precision Thiele equation approach* model (s-HPTEA), as it takes into account the whole

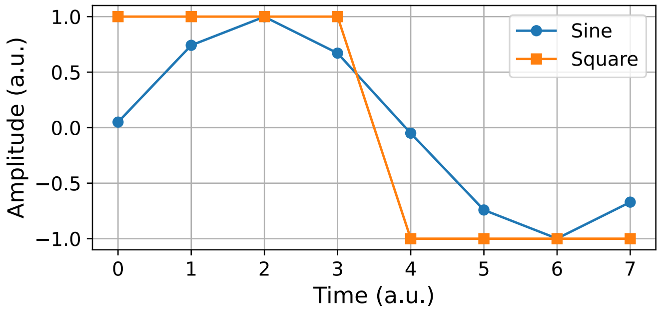

FIG. 1. Sine and square input signals used for benchmark. Note that the sine period is slightly offset in order to avoid having two samples at $y = 0$.

complexity of the vortex core dynamics.

$$s(t) = \frac{s_0}{\sqrt[n]{\left(1+\frac{s_0^n}{\alpha/\beta}\right)\exp(-n\alpha t)-\frac{s_0^n}{\alpha/\beta}}} \tag{11}$$

These two models, on top of being extremely fast to compute using a standard computer compared to micromagnetic simulations, yield highly accurate results thanks to the combination with micromagnetic simulations data. They were hence benchmarked using a simple machine learning task of waveform recognition.

The benchmark task consisted in the classification of sine and square periods composed of 8 samples (Fig. 1). To do so, a STVO-based neural reservoir [2–5, 24] composed of 24 different neurons was designed. By using time multiplexing, the neural network was emulated with only one STVO [9]. Instead of connecting 24 different STVOs in space to compose the network, the unique STVO successively played the role of 24 different neurons connected in time. This technique mainly allows to simplify the setup as the influence of the interactions between neighboring STVOs on their cognitive performance is not understood enough at the moment to be simulated reliably. The intrinsic dynamics of the STVO allowing to generate the output signal was modeled using the two models from Eq. (9) and Eq. (11) successively, allowing to compare their respective performance.

To train the network, a database of 80 sine periods and 80 square periods arranged in an alternate fashion was used, and the training procedure described in Ref. [18] was followed. For the testing, a similar yet randomly arranged database was preferred. The target related to a sine (resp. square) sample is the value 1 (resp. -1). To perfectly classify a given signal, the 8 samples that compose it must be classified correctly by the neural network. As any intermediate value between 1 and -1 can be returned by the neural network, any positive (resp. negative) output value was considered as the result of the detection of a sine (resp. square) sample. In the cases where the neural network was not able to yield a conclusive estimation (*i.e.*, the returned value was numerically considered as 0, making the decision uncertain), the output value was chosen randomly between 1 and -1 to implement random choice.

The classification result yielded by the neural network was constructed in two different ways, as presented in Ref. [18]. The τ-Wise (TW) approach consists in treating each of the 8 samples of a given period independently. The accuracy is thus a value between 0% if none of the samples was correctly recognized, and 100% if all the samples were correctly recognized (see Fig. 2, top). This allows to assess the performance of the neural network at recognizing sometimes very small partial inputs of data (in this case one eighth of a period). The Winner-Takes-All (WTA) method involves averaging the classification of the 8 samples of a period before choosing the value between 1 and -1 that is the closest to this average. This leads to an accuracy of 1 if the final value corresponds to the expected target, or 0 if not (see Fig. 2, bottom). This technique allows to absorb any small inaccuracies that may occur during the recognition of a period by considering it globally, hence leading to a slightly better accuracy than with the TW approach.

The geometry of a known experimental STVO was fully mimicked during the simulations. The diameter of the STVO was fixed to $d = 200$ nm, while its dc resistance R_{osc} was set to 140.6 Ω, accordingly to the values presented in Ref. [9, 10, 18]. The chirality of the STVO [22] was fixed to $+1$ during all the simulations to ensure the consistency of the results. However, all the calculations and results are extendable to the other chirality (-1) by using the corresponding constants [22].

The dc bias current intensity, or working current intensity I_{w} is used to trigger the gyrotropic motion of the vortex core. The input signal is added to it before entering the STVO. The value of I_{w} is important as it defines the regime in which the STVO will operate, and hence influences the way the data is processed by the STVO. It is represented by the black line in Fig. 3. Most of the time, I_{w} was set to $1.986 = 1.05 \times I_{\mathrm{cr1}}$ mA, with I_{cr1} the first critical current intensity [22]. However this value can actually be swept across a range of values in order to assess the influence of I_{w} on the results of the neural network during the benchmark task. The power of the input signal can be written as in Eq. (12) and Eq. (13).

$$P_{\mathrm{s}} = R_{\mathrm{osc}} I_{\mathrm{w}}^2 \qquad \text{(W)} \tag{12}$$

$$= 10 \times \log_{10}\left(R_{\mathrm{osc}} I_{\mathrm{w}}^2\right) \qquad \text{(dB)} \tag{13}$$

The amplitude of the input signal was scaled up to $\Delta V =$ 150 mV (centered on the working voltage derived from I_{w}, R_{osc} and Ohm's law). It is represented by the red interval around the I_{w} line in Fig. 3.

The sampling rate of the input signal was characterized with a time constant D_{t} of 50 ns. This parameter must also be chosen wisely as the transient state of the vortex core dynamics is the main contribution to the non-linear treatment of the data. Hence, a too small D_{t} will not allow to sufficiently leverage the transient state of the dynamics, while a too long D_{t} will lead to the saturation of the regime into the steady-state, hence decreasing the efficiency of the data treatment.

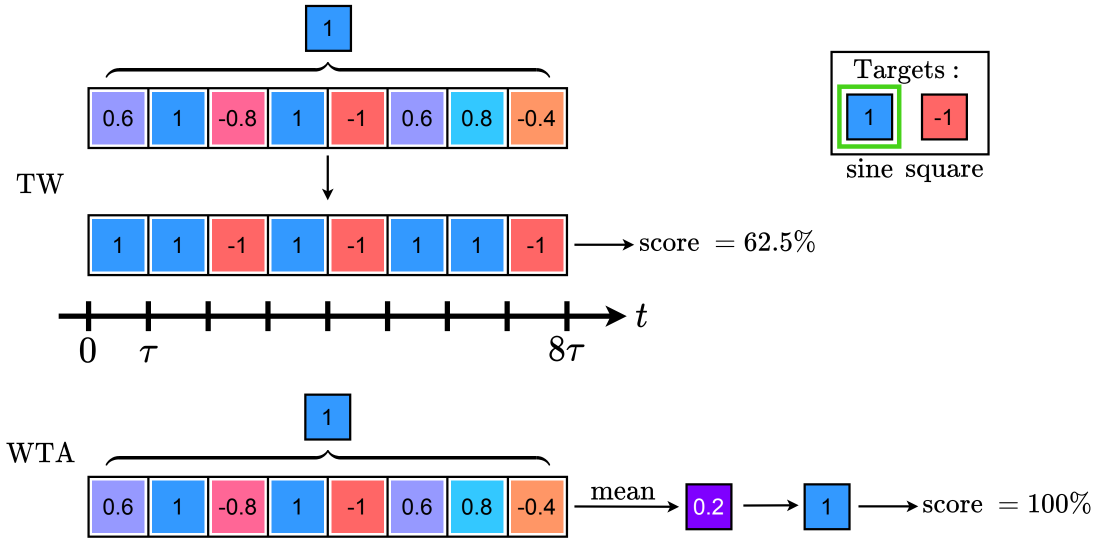

FIG. 2. Distinction between the TW and WTA approaches. The first and last arrays represent the result obtained by applying a final linear transformation on the output of the reservoir for a sine signal of length 8τ. The TW approach treats each sample of the signal independently, leading to an accuracy between 0% and 100%. The WTA approach absorbs the errors occurring in the recognition of the whole signal by averaging the results, leading to an accuracy of 100%.

White noise from various sources can be found in the experimental system under the form of thermal, electrical or magnetic noise. To consider the noise from all these sources as a single resultant quantity, an average peak-to-peak noise voltage amplitude of 50 mV is defined (corresponding to the blue intervals in Fig. 3). The related standard deviation σ can be retrieved using the $68-95-99.7$ rule and Eq. (14).

$$\sigma \simeq \frac{\Delta V_{\mathrm{noise}}}{6\sqrt{R_{\mathrm{osc}}}} \quad (\mathrm{W}^{1/2}) \tag{14}$$

A random signal normally distributed accordingly to σ and centered on $\mu = 0$ mV is then added to the input signal. The power of the noise can then be expressed as Eq. (15), Eq. (16) and Eq. (17). In practice, the noise in the input signal is negligible and all the noise originates from the STVO. However, as the analytical models do not model this internal noise, it has to be artificially added to the input signal.

$$\begin{aligned} P_{\mathrm{n}} &= \sigma^2 && (\mathrm{W}) && (15)\\ &= 10\times\log_{10}\left(\sigma^2\right) && (\mathrm{dB}) && (16)\\ &= 20\times\log_{10}(\sigma)+30 = -33.1 && (\mathrm{dBm}) && (17)\end{aligned}$$

The resulting signal-to-noise ratio can be computed using Eq. (18), Eq. (19) and Eq. (20). In the base case related to Fig. 3, it is equal to 30.5 dB. The level of noise can also be swept on a defined range to assess its influence on the accuracy of the recognition.

$$\begin{aligned} \mathrm{SNR} &= \frac{R_{\mathrm{osc}} I_{\mathrm{w}}^2}{\sigma^2} = \frac{36\times R_{\mathrm{osc}}^2 I_{\mathrm{w}}^2}{\Delta V_{\mathrm{noise}}^2} && (/) && (18)\\ &= 10\times\log_{10}\left(\frac{36\times R_{\mathrm{osc}}^2 I_{\mathrm{w}}^2}{\Delta V_{\mathrm{noise}}^2}\right) && (\mathrm{dB}) && (19)\\ &= 20\times\log_{10}\left(\frac{6\times R_{\mathrm{osc}} I_{\mathrm{w}}}{\Delta V_{\mathrm{noise}}}\right) && (\mathrm{dB}) && (20)\end{aligned}$$

The addition of all these contributions to the effective current density signal injected into the STVO has to be sanity-checked before every simulation. Indeed, if it exceeds the second critical current density J_{cr2} [22] the vortex state may be expelled out of the STVO, restoring an uniform magnetization and making the STVO useless for the recognition.

The results of the recognition were analyzed through two indicators: the accuracy and the root-mean-square of the error (RMSE) between the expected and actual outputs T_σ and $\hat{T}_\sigma$ (Eq. 21). The latter indicator was used as the accuracy was close to 100% in the large majority of the cases due to the low complexity of the task. High RMSE values indicate a non-optimal recognition even if the classification is correct. These indicators were averaged over all the 80 signals of the testing database.

$$\mathrm{RMSE} = \sqrt{\overline{\left(T_\sigma - \hat{T}_\sigma\right)^2}} \tag{21}$$

Due to the high throughput of the simulations allowed by the new models, two parametric studies have been performed. The first one consisted in a sweep of the working current intensity I_{w} to investigate the influence of the operat-

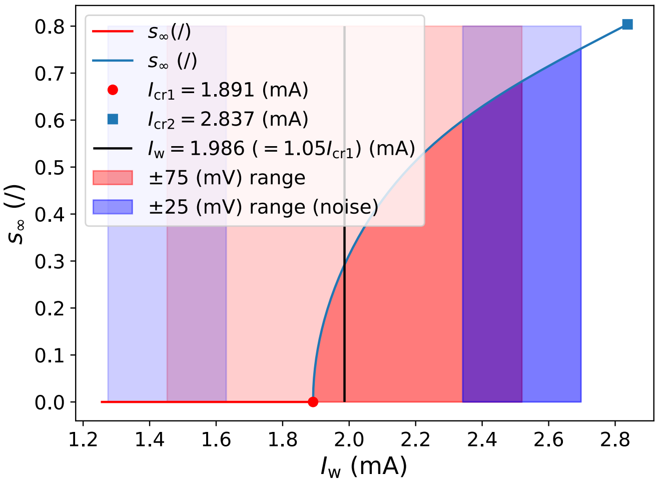

FIG. 3. Example of the current map and the range sounded by the dynamics of the oscillator. The black line corresponds to the working current intensity I_w, the red range corresponds to a input voltage range of $\Delta V = 150$ mV, and the blue ranges correspond to an additional noise voltage range of $\Delta V_{noise} = 50$ mV. The curve is the steady-state reduced position of the vortex core s_∞ reached for each input current intensity.

ing regime and the corresponding non-linearity on the treatment of the data. The working current intensity was swept from $1.001 \times I_{cr1}$ to the maximum allowed working current intensity $I_{w,max}$ defined in Eq. (22), ensuring that the total injected current intensity was not exceeding the second critical current intensity I_{cr2}.

$$I_{w,max} = I_{cr2} - \frac{\Delta V + \Delta V_{noise}}{2R_{osc}} \tag{22}$$

The other operating parameters are listed in Table II. For each value in the range swept, the accuracy and the RMSE were computed for both TW and WTA approaches, and so for both s-LOTEA and s-HPTEA models. To avoid the random fluctuations introduced with the background noise, the results were averaged over 200 simulations for each value of the sweep range. Note that the SNR also increases to a lesser extent during the sweep of I_w. Indeed, as I_w was swept from $1.001 \times I_{cr1}$ to $I_{w,max}$, the SNR was swept between 30.1 and 33.6 dB accordingly to Eq. (20).

The second parametric study consisted in a sweep of the signal-to-noise ratio (SNR) at a given working current intensity. For a given value of the SNR (in dB), an additive Gaussian white noise of the corresponding amplitude was added to the signal (as the blue areas in Fig. 3). A SNR of 0 dB corresponds to the case where the power of the input signal is equal to that of the added white noise, while positive (resp. negative) values correspond to the case were the power of the signal is higher (resp. lower) than that of the added noise. The SNR was swept from -20 dB to 100 dB, and the other operating parameters are the same as the one listed in Table II (note however that in this case, ΔV_{noise} is thus no longer constant, and the working current intensity I_w if fixed to $1.05 \times I_{cr1} = 1.986$ mA). The same metrics as in the first parametric study (*i.e.* the accuracy and the RMSE) were computed and averaged over 200 simulations. The case where SNR ≤ 0 dB is obviously not likely to happen in practice as it would mean that one expects to successfully classify random signals, but was nevertheless investigated for reasons detailed further.

TABLE II. Input parameters for the working current intensity parametric sweep. Note that the amplitude of the noise is a statistical value derived from the $68 - 95 - 99.7$ rule.

Parameter	Notation	Value	
DC resistance	R_{osc}	140.6	Ω
Chirality	C	+1	
Sampling rate	D_t	50	ns
Amplitude of the input signal	ΔV	150	mV
STVO diameter	d	200	nm
Amplitude of the noise	ΔV_{noise}	50	mV
		-33.1	dBm

The third and last task to which our new models were applied was the same speech recognition task as in Ref. [18]. This was meant to compare the simulated results with experimental measurements. To do so, the same database and code were used, and a similar neural network was designed. Only the non-linear treatment of the data was adapted with the new models.

The SNR of the experimental STVO used in Ref. [18] was estimated. The noise in the input signals was considered negligible and the estimator $\widehat{\text{SNR}}$ was computed as in Eq. (23), Eq. (24) and Eq. (25)

$$\widehat{\text{SNR}} = \frac{\widehat{P}_{signal}}{\widehat{P}_{noise}} \tag{23}$$

$$= \frac{\widehat{V}^2_{\text{RMS, signal}}}{\widehat{V}^2_{\text{RMS, noise}}} \tag{24}$$

$$= \frac{\overline{\left(\widehat{V}^2_{signal}\right)}}{\overline{\left(\widehat{V}^2_{noise}\right)}} \tag{25}$$

where $\widehat{V}_{signal}$ and $\widehat{V}_{noise}$ are estimations of the amplitude of the signal and the noise. Those were retrieved using the amplitude of the raw output signal V_{AVG1} and the average of the output signal over 16 measurements V_{AVG16} (see Eq. (26) and Eq. (27)). Due to the different levels of noise in these two output signals, the quality of their further classification is expected to be significantly different.

$$\widehat{V}_{signal} \approx V_{AVG16} \tag{26}$$

$$\widehat{V}_{noise} \approx V_{AVG1} - V_{AVG16} \tag{27}$$

TABLE III. Results of the benchmark task for the s-LOTEA and the s-HPTEA models averaged over 2000 simulations using the parameters related to Fig. 3. The bold values correspond to the best performance (*i.e.* highest accuracy or lowest RMSE) between the two models.

	Metrics	s-LOTEA	s-HPTEA
Training	Accuracy (WTA)	99.99%	**100%**
	Accuracy (TW)	99.77%	**99.94%**
	RMSE (WTA)	0.235	**0.198**
	RMSE (TW)	0.350	**0.300**
Testing	Accuracy (WTA)	**99.82%**	99.73%
	Accuracy (TW)	99.26%	**99.39%**
	RMSE (WTA)	0.278	**0.245**
	RMSE (TW)	0.402	**0.348**

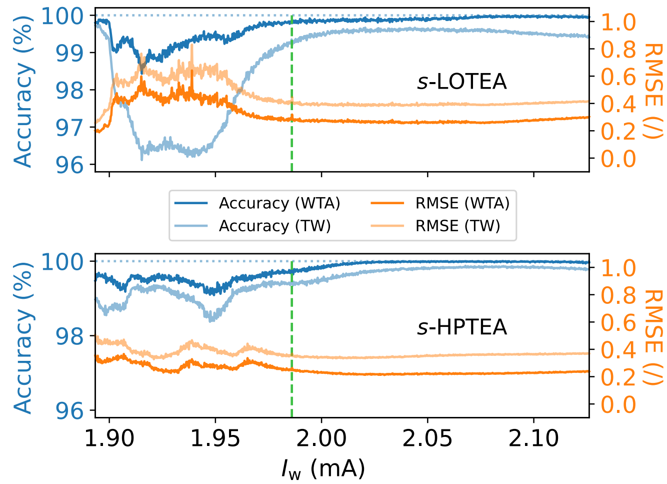

FIG. 4. Test accuracy and RMSE of the neural network emulated by a STVO, simulated using the s-LOTEA model (top) and the s-HPTEA model (bottom) during the parametric sweep of the working current intensity, averaged over 200 simulations. The green dashed vertical lines represent the working current intensity used in the base case (1.986 mA).

RESULTS AND DISCUSSION

The comparison between the results of the s-LOTEA and the s-HPTEA models during the benchmark task, averaged over 2000 simulations, is presented in Table III. Note that the two models are practically equally fast. Concerning the performance at the benchmark task, one can observe that in all of the cases but one, the s-HPTEA model yields slightly better results than the s-LOTEA model. The averaging of the results allows to state that these differences are unlikely to be randomly due to the simulated noise but rather to the models themselves. More specifically, this is due to the better description of the complexity of the vortex core dynamics in the s-HPTEA model. The s-HPTEA model, in addition to being the most accurate so far, thus also yields the best results when performing the benchmark task. This highlights the useful role of the STVO dynamics complexity into their performance as hardware neurons. In a more general way, it can be seen that the accuracy is extremely close to that of a perfect recognition, while needing a minimal amount of simulation time. Indeed, the training of the neural network with 80 signals and the inference of 80 other signals for testing took on average 0.7 s on a computer equipped with a standard Intel Core i7 processor. It is estimated that the same process would require about 50 years of computational time to complete using full-MMS simulations.

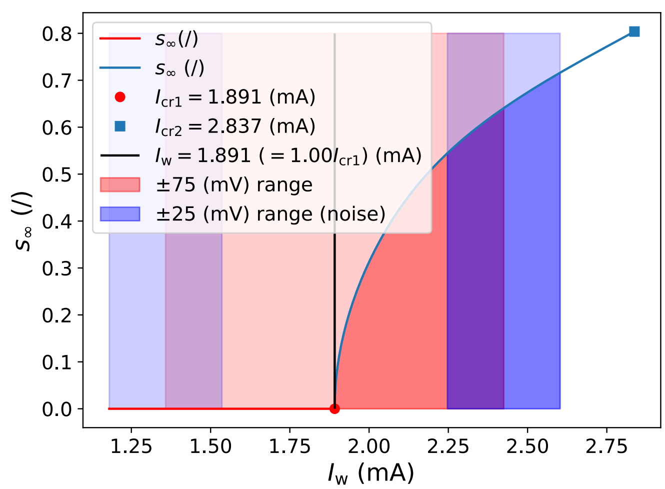

FIG. 5. Current map and range sounded by the dynamics of the oscillator when $I_w = I_{cr1}$. The signal has 50% chance to lie below I_{cr1} and to prevent the triggering of the STVO dynamics.

Influence of the working current intensity

The results obtained for the parametric sweep of the working current intensity with the two models are displayed in Fig. 4. It can be seen that for higher working current intensities, the performance of the neural network gets progressively better. Indeed, the accuracy reaches an upper asymptote at 100% and the RMSE decreases monotonically to a lower asymptotic value. This observation is valid for both models. It means that the regime in which the STVO operates when submitted to higher bias current intensities is beneficial for the recognition. This is due to the fact that the behavior of the STVO is less linear at higher current intensities, allowing a better quality of data processing [18]. This can be observed both under the physical and mathematical points of view. Physically, this is explained by the fact that when I_w decreases, the probability of the (noisy) signal to lie below the first critical current intensity I_{cr1} increases. Hence, the signal has a lower probability of triggering the vortex core oscillations required for the effective recognition of the data. For example, if $I_w = I_{cr1}$ as in Fig. 5, the signal has only 50% chance to lie above I_{cr1} and to induce STVO oscillations. This results in a decrease of the cognitive performance that can be seen at the leftmost end of Fig. 4.

Mathematically, this can be interpreted by considering the

TABLE IV. Results of the benchmark task for the s-LOTEA and the s-HPTEA models averaged over 2000 simulations when the input signal completely lies below I_{cr1}.

	Metrics	s-LOTEA	s-HPTEA
Training	Accuracy (WTA)	50.00%	50.00%
	Accuracy (TW)	50.00%	50.00%
	RMSE (WTA)	1.000	1.000
	RMSE (TW)	1.000	1.000
Testing	Accuracy (WTA)	50.00%	100.00%
	Accuracy (TW)	50.00%	100.00%
	RMSE (WTA)	1.000	1.000
	RMSE (TW)	1.000	1.000

s_∞ curve represented in red and blue in Fig. 3 and Fig. 5. Indeed, under I_{cr1} the vortex core is in the resonant state and its final reduced position s_∞ is equal to 0. As $s(t)$ is the effective mapping function that allows the treatment of the input data, any data point lying under I_{cr1} is mapped to 0, and cannot be made good use of to train the network non-linearly. This can be confirmed by considering the performance of the network when all the signal lies below I_{cr1}. In this situation, the signal is not able to trigger the oscillations of the vortex core and the input signal is linearly mapped to 0. An accuracy corresponding to random choice, *i.e.* 50%, is hence expected. This is verified is Table IV. This phenomenon is made clearly visible in the GIF attached in the supplementary material.

More generally, it can be noticed that the WTA approach systematically yields better results (*i.e.* higher accuracy and lower RMSE) than the TW approach as explained before. Furthermore, it can also be seen that the asymptotic values obtained with the s-HPTEA model are always better than that obtained with the s-LOTEA model. Note however that this observation may not be valid for lower current intensity values. For example at the working current intensity used for the base case (1.896 mA, see the green dashed vertical line in Fig. 4), the accuracy obtained with the WTA approach is higher when using the s-LOTEA model than when using the s-HPTEA model. This implies the existence of complex discrepancies between the dynamics modeled by the two models. All these observations show an undoubted agreement with the results presented in the lower half of Tab. III, highlighting the consistency of the simulations.

The existence of an optimal input current intensity is also suspected. As a matter of fact as I_{w} increases, the probability that the noise represented by the leftmost blue interval in Fig. 3 and Fig. 5 lies above I_{cr1} increases as well. As a reminder, these blue intervals are $\Delta V_{\mathrm{noise}}$ wide, and $\Delta V_{\mathrm{noise}}$ is approximately equal to $6\sigma\sqrt{R_{\mathrm{osc}}}$ as stated in Eq. (14). Noisy outliers are thus allowed to exceed I_{cr1}. This noise has a detrimental influence on the vortex core dynamics and hinder the network performance as it will be shown later. However this decrease of the performance at high input current intensities is limited. This is due to I_{w} being limited by $I_{\mathrm{w,max}}$ (see Eq. (22)), hence also limiting the probability of noisy data to reach or exceed I_{cr1}.

TABLE V. Coefficients and maximum relative error of the generalized logistic approximations of the accuracy reached with respect to the SNR (see Eq. (28) and Fig. 6).

	s-LOTEA		s-HPTEA	
	WTA	TW	WTA	TW
Q	553	214	1180	259
B	0.33	0.28	0.39	0.31
ν	1.74	1.39	1.49	1.07
max(RE)	2.9%	2.4%	2.7%	2.6%

This kind of study demonstrates the high value of our new analytical models. Those can be used to guide the design of an experimental system, by specifying the optimal working current intensity required to reach a given accuracy. In our case, I_{w} should be about 2.05 mA in order to reach an accuracy of 99.99% when considering the s-HPTEA model.

Influence of the noise

The results of the parametric study on the SNR are displayed in Fig. 6. It can be noticed that a sigmoid-like curve is obtained when plotting the accuracy with respect to the SNR. For positive SNRs, the accuracy reaches 100% due to the progressively less noisy system. As the SNR decreases, the accuracy drops to 50%. This accuracy corresponds to random choice between the two categories (sine and square). This is due to the noise decreasing the quality of the dynamics down to the point where no usable features can be found in the signals and leveraged by the neural network for the classification. The resulting curves were fitted using a generalized logistic approximation such as Eq. (28), whose coefficients and maximum relative errors are presented in Table V.

$$\mathrm{ACC}(\mathrm{SNR}) = 50 + \frac{50}{\left(1+Q\exp(-B\,\mathrm{SNR})\right)^{1/\nu}}\% \qquad (28)$$

These relations, which would not have been possible to express accurately without the new models, could help to estimate precious information about a physical prototype. For example the expected accuracy for this recognition task can be retrieved once the value of the SNR of the system has been estimated. Alternatively, these relations could also be used to know the minimum SNR value required to reach a given accuracy level. For example, by considering the s-HPTEA model, it is possible to state that the SNR must be at least 22.77 dB to reach an accuracy of 95% with the WTA approach. Considering a working current intensity of 1.986 mA (as in the base case), this corresponds to a noise whose average peak-to-peak amplitude is about 122 mV.

The interpretation of the RMSE plots is somewhat less trivial. Under a SNR of about 20 dB, the RMSE explodes and has to be truncated to 1.00. Indeed, as the random fluctuations introduced with the noise become more and more predominant for lower SNRs, the resulting signal becomes less and

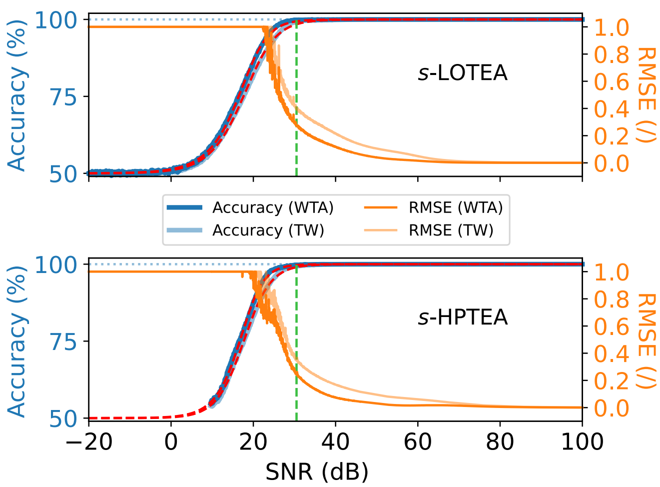

FIG. 6. Test accuracy and RMSE of the neural network emulated by a STVO, simulated using the *s*-LOTEA model (top) and the *s*-HPTEA model (bottom) during the parametric sweep of the system SNR, averaged over 200 simulations. The RMSE values were truncated to 1.00 due to high RMSE for negative SNRs. The red dashed lines represent the piece-wise generalized logistic approximations from Eq. (28) and Table V. The green dashed vertical lines represent the SNR simulated in the base case (30.5 dB).

less similar to the bounded signals that were used to train the network (Fig. 1). The occurrence of these unexpected high-amplitude values in the network leads to a steep increase of the RMSE. As the SNR increases above 20 dB, the progressively cleaner dynamics leads to a monotonous decrease of the RMSE as expected.

There does not seem to be any differences between the plots of the two models in Fig. 6 when the noise is moderate or negligible (SNR $>$ 10 dB). However one can observe that there are no data for the accuracy under 10 dB with the *s*-HPTEA model due to the simulations crashing. It is suspected that the *s*-HPTEA model is more sensitive to noise due to its inherent higher-order dynamics.

Comparison with experimental results

The two new models were used to perform the same speech recognition task as in Ref. [18]. This task consists in classifying spoken digits from 0 to 9 while involving various levels of non-linearity in the pre-treatment of the data. Indeed, the audio signals can be pre-processed using acoustic filters with different degrees of non-linearity in order to ease their further classification by the neural network. These acoustic filters allow to non-linearly extract acoustic features from the input signal by decomposing it into a given set of frequency channels. Among the non-linear filters used, the Mel-frequency cepstral coefficients (MFCC) and Lyon's cochlear model (cochleagram) are based on mimicking the filtering that occurs biologically [18]. The third non-linear filter, Spectro HP, is a custom non-linear transformation of the complex decomposition of the data. The main result of this study is the fact that when the level of non-linearity of the acoustic filter applied on the input data increases, the contribution of the STVO-based neural network in the processing of the data decreases. This reinforces the idea that the effective role of the neural network is to process the data non-linearly, and that standalone non-linear acoustic filters can already achieve high levels of recognition accuracy without the help of a neural network [18]. It was also observed that in some cases, the simulated results (with the phenomenological model based on the non-linear magnetic oscillator theory) were surprisingly lower than the experimental ones, hence motivating the development of the more accurate physical models presented in this work.

TABLE VI. Estimated SNR for the experimental measurements using different non-linear acoustic filters for speech recognition (data from Ref. [18]).

Non-linear filter	**Estimation of the SNR ($\widehat{SNR}$)**
MFCC	18.76 dB
Cochleagram	15.59 dB
Spectro HP	19.78 dB

The results obtained for the training and testing phases are displayed in Fig. 7. In general, a very good agreement between the experimental results and the the results obtained with our two analytical models is observed. It can be seen that in all the cases but one, the results obtained with the two new models are higher or equal to the experimental ones, which is expected and supports their validity.

The SNRs estimated using Eq. (23) for the experimental measurements performed using the MFCC, cochleagram and Spectro HP filters are presented in Table VI. These positive values induce that one can expect to observe an improvement of the metrics (accuracy and RMSE) between the classification of the raw V_{AVG1} output signals and the less noisy V_{AVG16} output signals. This expectation has been confirmed with the experimental measurements related to the three acoustic filters. As a matter of fact, the accuracy is systematically higher during the classification of the averaged V_{AVG16} signals than for the raw V_{AVG1} signals, and the RMSE systematically lower. The only cases where the performance are not improving is when the accuracy is already equal to 100% with the V_{AVG1} signals, or when the RMSE has reached a plateau such as the one showed at high SNRs in Fig. 6. These observations validate the earlier results obtained from the parametric sweep of the SNR, *i.e.* the quality of the recognition improves significantly at higher SNRs.

CONCLUSION

Two new models based on the Thiele equation approach were developed to simulate the dynamics of STVOs. The combination of mathematical expressions with numerical results obtained with MMS allowed to obtain a physical descrip-

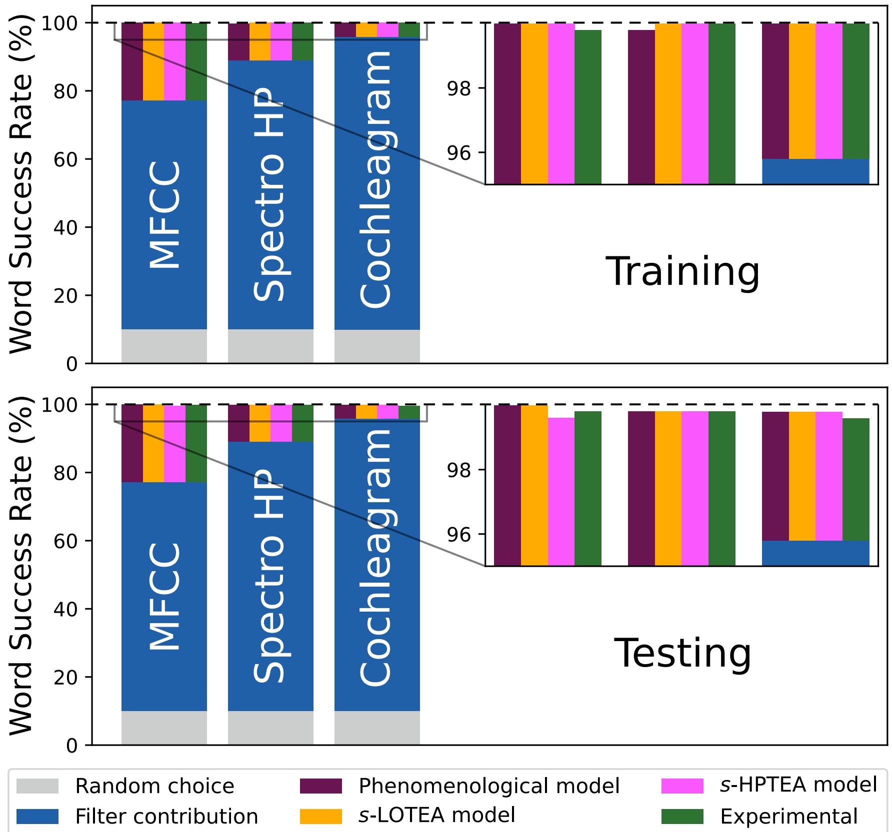

FIG. 7. Comparison between the different contributions to the accuracy (or Word-Success-Rate, WSR), obtained with the WTA approach during the training (top) and testing (bottom) phases, with different acoustic filters. The green columns are from Ref. [18]. The purple, orange and pink columns represent respectively the accuracy obtained with the phenomenological model, the s-LOTEA model, and the s-HPTEA model.

tion of the vortex core dynamics under a given input signal. The resulting accuracy is at the same level as MMS. Additional mathematical and numerical adjustments were brought to allow the analytical resolution of the models and accelerate the simulations up to 9 orders of magnitude compared to MMS. One of the model (s-LOTEA) truncates the transient dynamic factor $\Gamma(s)$ representing the non-linearity of the dynamics to the second order. The other model (s-HPTEA) allows to take into account the whole complexity of the dynamics non-linearity. A benchmark task consisting in the classification of sine and square periods was designed. It was observed that the simulations ruled by the two new models require a similar amount of time, but the s-HPTEA model yields slightly better results due to the consideration of the higher-order complexity of the dynamics non-linearity. The speed of the simulations allowed to perform two parametric studies about the performances of the network during the benchmark task, with respect to the working current intensity I_{w} and the level of noise in the system. The first study allowed to determine an optimal operating current intensity for the use of a experimental setup for this given task. The second study allowed to drawn unprecedented relations between the accuracy and the signal-to-noise ratio of the system. These two studies would have been impossible to perform in practice using MMS, hence highlighting the value of our analytical models. Finally, a comparison was made between the two new models and the values obtained for a speech recognition task in Ref. [9, 18]. A very good agreement is obtained between the new models and the experimental results. In almost all cases, the simulated results are superior to the experimental results, which is expected but was not seen in Ref. [18]. An improvement of the recognition quality with the SNR of the system is also observed experimentally.

The use of our new models based on the physical description of STVO dynamics is expected to lead to a major development in the simulation of STVO-based neural networks. The huge acceleration factor induced by their analytical resolution will allow to simulate larger and more complex networks, and to progressively get rid of the time multiplexing technique. This will improve the efficiency of the simulations of said neural networks, and will open the path to the design of more complex experimental setups.

ACKNOWLEDGEMENTS

Computational resources have been provided by the Consortium des Équipements de Calcul Intensif (CÉCI), funded by the Fonds de la Recherche Scientifique de Belgique (F.R.S.-FNRS) under Grant No. 2.5020.11 and by the Walloon Region. F.A.A. is a Research Associate and S.d.W. is a FRIA grantee, both of the F.R.S.-FNRS. The experimental data originates from the measurements by Jacob Torrejon, Mathieu Riou, and F.A.A. while working in Julie Grollier's group at Unité Mixte de Physique CNRS/Thales in France and the samples were produced at AIST (Spintronics Research Center, Tsukuba) in Japan under the responsibility of our colleagues Sumito Tsunegi, Kay Yakushiji, Akio Fukushima, Hitoshi Kubota, and Shinji Yuasa.

AUTHOR'S CONTRIBUTION

The study was designed by F.A.A. who created the analytical foundation related to the Thiele equation approach with the assistance of S.d.W. and C.C.. F.A.A. developed the two analytical models and combined them with numerical data obtained by micromagnetic simulations performed by S.d.W.. A.M. designed and performed the benchmark tasks, the parametric studies, and compared the numerical results with the experiment data. A.M. wrote the core of the manuscript and all the other co-authors (F.A.A., S.d.W., C.C., and J.W.) contributed to the text as well as to the analysis of the results.

REFERENCES

* flavio.abreuaraujo@uclouvain.be; https://flavio.be

[1] G. Indiveri and T. K. Horiuchi, Frontiers in neuroscience **5**, 118 (2011).

[2] Y. Paquot, J. Dambre, B. Schrauwen, M. Haelterman, and S. Massar, in *Nonlinear optics and applications IV*, Vol. 7728 (SPIE, 2010) pp. 58–69.

[3] Y. Paquot, F. Duport, A. Smerieri, J. Dambre, B. Schrauwen, M. Haelterman, and S. Massar, Scientific Reports **2**, 1 (2012).

[4] L. Larger, M. C. Soriano, D. Brunner, L. Appeltant, J. M. Gutiérrez, L. Pesquera, C. R. Mirasso, and I. Fischer, Optics Express **20**, 3241 (2012).

[5] L. Larger, A. Baylón-Fuentes, R. Martinenghi, V. S. Udaltsov, Y. K. Chembo, and M. Jacquot, Physical Review X **7**, 011015 (2017).

[6] B. J. Shastri, A. N. Tait, T. F. de Lima, W. H. Pernice, H. Bhaskaran, C. D. Wright, and P. R. Prucnal, Nature Photonics **15**, 102 (2021).

[7] S. H. Jo, T. Chang, I. Ebong, B. B. Bhadviya, P. Mazumder, and W. Lu, Nano letters **10**, 1297 (2010).

[8] J. Grollier, D. Querlioz, K. Camsari, K. Everschor-Sitte, S. Fukami, and M. D. Stiles, Nature electronics **3**, 360 (2020).

[9] J. Torrejon, M. Riou, F. Abreu Araujo, S. Tsunegi, G. Khalsa, D. Querlioz, P. Bortolotti, V. Cros, K. Yakushiji, A. Fukushima, *et al.*, Nature **547**, 428–431 (2017).

[10] M. Riou, J. Torrejon, B. Garitaine, F. Abreu Araujo, P. Bortolotti, V. Cros, S. Tsunegi, K. Yakushiji, A. Fukushima, H. Kubota, *et al.*, Physical Review Applied **12** (2019), 10.1103/physrevapplied.12.024049.

[11] D. Marković, N. Leroux, M. Riou, F. Abreu Araujo, J. Torrejon, D. Querlioz, A. Fukushima, S. Yuasa, J. Trastoy, P. Bortolotti, *et al.*, Applied Physics Letters **114**, 012409 (2019).

[12] K. Yogendra, D. Fan, and K. Roy, IEEE Transactions on Magnetics **51**, 1–9 (2015).

[13] M. Riou, F. A. Araujo, J. Torrejon, S. Tsunegi, G. Khalsa, D. Querlioz, P. Bortolotti, V. Cros, K. Yakushiji, A. Fukushima, *et al.*, in *2017 IEEE International Electron Devices Meeting (IEDM)* (IEEE, 2017) pp. 36–3.

[14] M. Riou, J. Torrejon, F. Abreu Araujo, S. Tsunegi, G. Khalsa, D. Querlioz, P. Bortolotti, N. Leroux, D. Marković, V. Cros, *et al.*, in *Reservoir Computing* (Springer, 2021) pp. 307–329.

[15] A. Vansteenkiste, L. Jonathan, M. Dvornik, M. Helsen, F. Garcia-Sanchez, and B. Van Waeyenberge, AIP Advances **4**, 107 (2014).

[16] F. Abreu Araujo, C. Chopin, and S. de Wergifosse, arXiv:2206.13596 (2022), 10.48550/arXiv.2206.13596.

[17] A. Slavin and V. Tiberkevich, IEEE Transactions on Magnetics **45**, 1875 (2009).

[18] F. Abreu Araujo, M. Riou, J. Torrejon, S. Tsunegi, D. Querlioz, K. Yakushiji, A. Fukushima, H. Kubota, S. Yuasa, M. D. Stiles, *et al.*, Scientific Reports **10** (2020), 10.1038/s41598-019-56991-x.

[19] X. Chen, F. Abreu Araujo, M. Riou, J. Torrejon, D. Ravelosona, W. Kang, W. Zhao, J. Grollier, and D. Querlioz, Nature communications **13**, 1 (2022).

[20] A. Thiele, Physical Review Letters **30**, 230 (1973).

[21] D. Huber, Physical Review B **26**, 3758 (1982).

[22] F. Abreu Araujo, C. Chopin, and S. de Wergifosse, Scientific Reports **12** (2022), 10.1038/s41598-022-14574-3.

[23] K. Y. Guslienko, O. V. Sukhostavets, and D. V. Berkov, Nanoscale research letters **9**, 1 (2014).

[24] B. Schrauwen, D. Verstraeten, and J. Van Campenhout, in *Proceedings of the 15th european symposium on artificial neural networks. p. 471-482 2007* (2007) pp. 471–482.